J|A|C|S
ARTICLES

Published on Web 09/08/2010

Dopant-Induced Shape Evolution of Colloidal Nanocrystals: The Case of Zinc Oxide

Yefeng Yang,[†] Yizheng Jin,[†,*] Haiping He,[†] Qingling Wang,[†] Yao Tu,[†] Huanming Lu,[‡] and Zhizhen Ye[†,*]

State Key Laboratory of Silicon Materials, Department of Materials Science and Engineering, Zhejiang University, Hangzhou 310027, P.R. China, and Ningbo Institute of Material Technology and Engineering, Chinese Academy of Sciences, Ningbo 315201, P.R. China

Received May 9, 2010; E-mail: yizhengjin@zju.edu.cn; yezz@zju.edu.cn

Abstract: The electrical, optical and other important properties of colloidal nanocrystals are determined mainly by the crystals' chemical composition, size and shape. The introduction of specific dopants is a general approach of modifying the properties of such nanocrystals in well-controlled ways. Here we show that in addition to altering the atomic composition of the nanocrystals the introduction of specific dopants can also lead to dramatic changes in morphology. The creation of Mg-doped ZnO nanocrystals provides an excellent example of this procedure; depending on the molar ratio of dopant precursor in the reagents, doped nanocrystals with well-defined shapes, from tetrapods to ultrathin nanowires, which exhibit tunable optoelectronic properties, are obtained for the first time. We find that the Mg dopants play an important role in the primary growth stage, resulting in initial growth seeds having diverse crystallographic structures, which are critical for the generation of doped nanocrystals with different shapes. We demonstrate that this "greener" synthetic scheme can be extended to other dopant systems and provides an attractive and effective strategy for fabricating doped ZnO nanocrystals with interesting compositional and spatial complexity.

Introduction

Doping that involves intentional incorporation of atoms or ions of specific elements into host lattices to generate materials with desirable functions is a widely applied technological process to control and manipulate the properties of semiconductors. Doping is essential for modern semiconductor industry. Doping is also expected to play a key role in the future nanoscience and nanotechnology by means of creating doped nanocrystals and nanostructures with unprecedented properties.[1−3]

Colloidal semiconductor nanocrystals are currently considered as an important class of materials both for fundamental studies and technological applications because of their unique combination of remarkable properties and nature of ease of fabrication and processing. Synthesis of colloidal nanocrystals aiming to precisely control the crystal's size, shape and composition, which determine electrical, optical and other properties of such materials, has advanced dramatically in recent years.[4−9] For many semiconductors, their dot-shaped nanocrystals have been prepared with precise control over size and size distribution.[6,10−13] A few techniques, including use of appropriate capping agents,[14] monomer activity-mediated kinetic growth,[15] solution−liquid−solid catalytic route,[16] seeded growth,[17] and oriented attachment of nanoparticles[18,19] have been developed to produce nanocrystals with anisotropic shapes, e.g., wires and tetrapods.

Doping, or alloying nanocrystals provides another fundamental approach to modify the properties of nanocrystals by means of tailoring the crystal's compositions.[1] A good example is ZnSe nanocrystals doped with Mn or Cu impurities which exhibit tunable emission in a considerable large optical window with high photoluminescence (PL) quantum yield and high

[†] Zhejiang University.
[‡] Chinese Academy of Sciences.

(1) Norris, D. J.; Efros, A. L.; Erwin, S. C. *Science* **2008**, *319*, 1776–1779.
(2) Cui, Y.; Lieber, C. M. *Science* **2001**, *291*, 851–853.
(3) Ayala, P.; Arenal, R.; Rummeli, M.; Rubio, A.; Pichler, T. *Carbon* **2010**, *48*, 575–586.
(4) Murray, C. B.; Norris, D. J.; Bawendi, M. G. *J. Am. Chem. Soc.* **1993**, *115*, 8706–8715.
(5) Peng, X. G.; Manna, L.; Yang, W. D.; Wickham, J.; Scher, E.; Kadavanich, A.; Alivisatos, A. P. *Nature* **2000**, *404*, 59–61.
(6) Murray, C. B.; Kagan, C. R.; Bawendi, M. G. *Annu. Rev. Mater. Sci.* **2000**, *30*, 545–610.
(7) Yin, Y. D.; Alivisatos, A. P. *Nature* **2005**, *437*, 664–670.
(8) Jun, Y. W.; Choi, J. S.; Cheon, J. W. *Angew. Chem., Int. Ed.* **2006**, *45*, 3414–3439.
(9) Peng, X. G. *Nano Res.* **2009**, *2*, 425–447.
(10) Peng, X.; Wickham, J.; Alivisatos, A. P. *J. Am. Chem. Soc.* **1998**, *120*, 5343–5344.
(11) Joo, J.; Na, H. B.; Yu, T.; Yu, J. H.; Kim, Y. W.; Wu, F.; Zhang, J. Z.; Hyeon, T. *J. Am. Chem. Soc.* **2003**, *125*, 11100–11105.
(12) Park, J.; Joo, J.; Kwon, S. G.; Jang, Y.; Hyeon, T. *Angew. Chem., Int. Ed.* **2007**, *46*, 4630–4660.
(13) Allen, P. M.; Liu, W. H.; Chauhan, V. P.; Lee, J.; Ting, A. Y.; Fukumura, D.; Jain, R. K.; Bawendi, M. G. *J. Am. Chem. Soc.* **2010**, *132*, 470–471.
(14) Manna, L.; Scher, E. C.; Alivisatos, A. P. *J. Am. Chem. Soc.* **2000**, *122*, 12700–12706.
(15) Peng, Z. A.; Peng, X. G. *J. Am. Chem. Soc.* **2002**, *124*, 3343–3353.
(16) Trentler, T. J.; Hickman, K. M.; Goel, S. C.; Viano, A. M.; Gibbons, P. C.; Buhro, W. E. *Science* **1995**, *270*, 1791–1794.
(17) Fiore, A.; Mastria, R.; Lupo, M. G.; Lanzani, G.; Giannini, C.; Carlino, E.; Morello, G.; De Giorgi, M.; Li, Y.; Cingolani, R.; Manna, L. *J. Am. Chem. Soc.* **2009**, *131*, 2274–2282.
(18) Pacholski, C.; Kornowski, A.; Weller, H. *Angew. Chem., Int. Ed.* **2002**, *41*, 1188–1191.
(19) Cho, K. S.; Talapin, D. V.; Gaschler, W.; Murray, C. B. *J. Am. Chem. Soc.* **2005**, *127*, 7140–7147.

resistance to photooxidation.[20,21] In another study, photovoltaic devices employing PbS_xSe_{1-x} nanocrystals exhibit better efficiencies than devices based on either pure PbS or pure PbSe nanocrystals.[22] Nanocrystals doped with magnetic centers, for example, Co-doped ZnO nanocrystals[23] and Mn-doped CdSe nanocrystals,[24] which may serve as key building blocks for spintronics, have also been fabricated. In the course of preparing this manuscript, we noticed that $NaYF_4$ nanocrystals could be rationally tuned in size, phase and upconversion emission color by introducing trivalent lanthanide dopant ions, such as Gd^{3+}, with defined concentrations up to 60 mol %, which were demonstrated by Wang et al.[25] More recently, Chen et al. found that the size and shape of alkaline-earth fluoride nanocrystals were modified through lanthanide doping.[26]

It is noteworthy that the definition of doping for the doped nanocrystals and for the semiconductor industry may be slightly different. In traditional semiconductor industry, doping means introduction of trace amount of impurities into extremely pure semiconductors. When dopant concentration is on the order of 1 per 10,000 atoms, the doping is referred to as heavy or high. If this description is applied to the doped nanocrystals, even a minimum level of doping, one single dopant atom in a nanocrystal shall be called heavy doping since the number of atoms contained in a nanocrystal is generally less than 10,000. In many publications of doped nanocrystals, doping simply refers to the incorporation of dopant atoms into the host crystal lattices. The dopant concentrations of the doped nanocrystals can be as high as a few percent, and in some cases, even over ten percent, which in fact form alloyed nanocrystals.[24,25,27−33] The concept of doping that is generally used for doped nanocrystals is adopted in the present study.

Knowledge on the formation of the doped nanocrystals is still limited although attempts aiming to investigate the underlying mechanisms that control doping have been reported in the literature. For instance, 'self-purification', a thermodynamic concept, was invoked to explain the low doping concentration in the case of Mn-doped CdSe nanocrystals.[34] Erwin et al. propose that for the Mn-doped II−VI nanocrystals doping is controlled by impurity adsorption on the nanocrystal surfaces.[35] The doping efficiencies of the Mn-doped II−VI nanocrystals are mainly determined by three factors: surface morphology, nanocrystal shapes, and surfactants in the growth solution. In a recent study, Chen et al. demonstrate that doping nanocrystals is complex and at least four individual processes that are strongly temperature-dependent are involved.[36] For the lanthanide-doped $NaYF_4$ nanocrystals, Wang et al. suggest that the influence of lanthanide doping strongly depends on the size and dipole polarizability of the substitutional dopant ions.[25] Despite these efforts, interactions between dopant ions and host lattices during the growth of doped nanocrystals are not fully understood. Studies on the effects of dopants in determining the shape of nanocrystals are rare.[37] As a consequence, shape control of doped nanocrystals[38] is much less developed in comparison with that of undoped nanocrystals.

Here, we show that in the synthesis of ZnO nanocrystals, introduction of Mg dopants leads to dramatic shape evolution in addition to the compositional variation of the resulting nanocrystals. Depending on the relative concentrations of the dopant precursor, Mg-doped ZnO nanocrystals with well-defined shapes, from tetrapods to ultrathin nanowires, which exhibit tunable optoelectronic properties, were obtained for the first time. The mechanism related to the shape evolution of the Mg-doped ZnO nanocrystals was explored. We further applied the principles developed for the Mg-doped ZnO nanocrystals to a variety of other dopants, creating doped ZnO nanocrystals with interesting compositional and spatial complexity.

Experimental Section

Materials. Zinc stearate ($Zn(St)_2$), magnesium stearate ($Mg(St)_2$), manganese acetate ($Mn(Ac)_2$), nickel stearate ($Ni(St)_2$), *n*-octadecane (tech 90%), and 1-octadecanol (ODA, 97%) were purchased from Alfa Aesar. Cadmium acetate dehydrate ($Cd(Ac)_2 \cdot 2H_2O$), trifluoroacetic acid (99%) and 1-octadecene (ODE, tech 90%) were purchased from Acros Organics. Stearic acid (HSt, 95%) was purchased from Aldrich. Ethyl acetate, toluene, chloroform, hexane, and methanol were analytical grade reagents (Sinopharm Chemical Reagent Co.). All chemicals were used as received.

Synthesis of Nanocrystals Starting with $Zn(St)_2$ and $Mg(St)_2$. We carried out a set of reactions starting with different relative concentrations of the dopant precursor in the reagents to explore the shape evolution of colloidal nanocrystals. In these reactions, the cation quantity which was the total amount of the Zn precursor, $Zn(St)_2$, and the Mg precursor, $Mg(St)_2$, was kept at 1 mmol. The molar ratios of $Mg(St)_2$:$Zn(St)_2$ were varied from 0:100% (pure $Zn(St)_2$) to 2:98%, 5:95%, 10:90%, 20:80%, 30:70%, 40:60%, 50:50%, 60:40%, 70:30%, 80:20%, 90:10% and 100:0% (pure $Mg(St)_2$), respectively. For the sake of simplicity, these reactions are named after the molar ratio of the Mg precursor. For instance, the 5% $Mg(St)_2$ reaction represents the reaction starting with 0.05 mmol of $Mg(St)_2$ and 0.95 mmol of $Zn(St)_2$.

An example of synthetic protocol for the Mg-doped ZnO nanocrystals follows: $Zn(St)_2$ (0.95 mmol), $Mg(St)_2$ (0.05 mmol), and 20 g of ODE were loaded in a 100 mL three-necked flask, degassed and heated to 270 °C under an argon flow. A separate solution of ODE (5 g) containing ODA (5 mmol) at 200 °C was rapidly injected into the reaction flask to generate nanocrystals. The

(20) Pradhan, N.; Goorskey, D.; Thessing, J.; Peng, X. G. *J. Am. Chem. Soc.* **2005**, *127*, 17586–17587.
(21) Pradhan, N.; Peng, X. G. *J. Am. Chem. Soc.* **2007**, *129*, 3339–3347.
(22) Ma, W.; Luther, J. M.; Zheng, H.; Wu, Y.; Alivisatos, A. P. *Nano Lett.* **2009**, *9*, 1699–1703.
(23) Schwartz, D. A.; Norberg, N. S.; Nguyen, Q. P.; Parker, J. M.; Gamelin, D. R. *J. Am. Chem. Soc.* **2003**, *125*, 13205–13218.
(24) Yu, J. H.; et al. *Nat. Mater.* **2009**, *9*, 47–53.
(25) Wang, F.; Han, Y.; Lim, C. S.; Lu, Y.; Wang, J.; Xu, J.; Chen, H.; Zhang, C.; Hong, M.; Liu, X. *Nature* **2010**, *463*, 1061–1065.
(26) Chen, D.; Yu, Y.; Huang, F.; Huang, P.; Yang, A.; Wang, Y. *J. Am. Chem. Soc.* **2010**, *132*, 9976–9978.
(27) Farvid, S. S.; Dave, N.; Wang, T.; Radovanovic, P. V. *J. Phys. Chem. C* **2009**, *113*, 15928–15933.
(28) Zeng, R. S.; Rutherford, M.; Xie, R. G.; Zou, B. S.; Peng, X. G. *Chem. Mater.* **2010**, *22*, 2107–2113.
(29) Li, Z.; Cheng, L. N.; Sun, Q.; Zhu, Z. H.; Riley, M. J.; Aljada, M.; Cheng, Z. X.; Wang, X. L.; Hanson, G. R.; Qiao, S. Z.; Smith, S. C.; Lu, G. Q. *Angew. Chem., Int. Ed.* **2010**, *49*, 2777–2781.
(30) White, M. A.; Ochsenbein, S. T.; Gamelin, D. R. *Chem. Mater.* **2008**, *20*, 7107–7116.
(31) Kwak, W. C.; Kim, T. G.; Chae, W. S.; Sung, Y. M. *Nanotechnology* **2007**, *18*, 205702.
(32) Nag, A.; Chakraborty, S.; Sarma, D. D. *J. Am. Chem. Soc.* **2008**, *130*, 10605–10611.
(33) Zhang, Q. A.; Sun, T.; Cao, F.; Li, M.; Hong, M. H.; Yuan, J. K.; Yan, Q. Y.; Hng, H. H.; Wu, N. Q.; Liu, X. G. *Nanoscale* **2010**, *2*, 1256–1259.
(34) Dalpian, G. M.; Chelikowsky, J. R. *Phys. Rev. Lett.* **2006**, *96*, 226802.
(35) Erwin, S. C.; Zu, L. J.; Haftel, M. I.; Efros, A. L.; Kennedy, T. A.; Norris, D. J. *Nature* **2005**, *436*, 91–94.
(36) Chen, D.; Viswanatha, R.; Ong, G. L.; Xie, R.; Balasubramaninan, M.; Peng, X. *J. Am. Chem. Soc.* **2009**, *131*, 9333–9339.
(37) Zu, L. J.; Norris, D. J.; Kennedy, T. A.; Erwin, S. C.; Efros, A. L. *Nano Lett.* **2006**, *6*, 334–340.
(38) Viswanatha, R.; Battaglia, D.; Curtis, M.; Mishima, T.; Johnson, M.; Peng, X. *Nano Res.* **2008**, *1*, 138–144.

reaction temperature, which dropped to ~248 °C due to the injection of ODA solution, was allowed to rise to 270 °C by heating in ~4 min and stabilized afterward. When the reaction was finished, the reaction mixture was cooled to room temperature by water bath. The resulting nanocrystals were precipitated by an excess of ethyl acetate and collected by centrifugation. Next the nanocrystals were dispersed in toluene and centrifuged to remove any insoluble species. After being washed several times with the use of toluene/methanol combinations, the purified nanocrystals were highly soluble in nonpolar solvents such as chloroform, toluene, and hexane.

Monitoring the Growth of the Doped Nanocrystals. The growth processes of the doped nanocrystals were monitored by UV−vis absorption spectra and transmission electron microscopy (TEM). For the 5% and 50% $Mg(St)_2$ reactions, aliquots were taken from the reaction solutions and mixed with hexane at an interval of 15 s after injections of alcohol solutions to initiate the reactions. The nanocrystals contained in the aliquots were purified by successive methanol/hexane extractions to obtain clear solutions which were used for UV−vis absorption and TEM measurements. The nanocrystals in the solution were precipitated, dissolved in hexane and filtered through 0.20 μm PTFE filters before preparing samples for elemental analyses.

Seeded Growth Experiment. A seeded growth experiment, which decoupled the formation of growth seeds and the incorporation of Mg^{2+} ions into the host lattices, was designed to study the doping effects on the growth of the nanocrystals. In a typical synthetic procedure, $Zn(St)_2$ (0.5 mmol) and 18.7 g of ODE were loaded in a 100 mL three-necked flask. The mixture was degassed and heated to 270 °C under an argon flow. A separate solution of ODA (5 mmol) in 5 g of ODE at 200 °C was quickly injected into the reaction flask to generate nanocrystals. After 4 min, an ODE solution (2.9 g of ODE) of $Mg(St)_2$ (0.5 mmol) at 270 °C was injected into the reaction flask. The reaction was extended for another 4 min. The seeded growth reaction was monitored by taking aliquots at different time intervals for UV−vis absorption and TEM measurements.

Synthesis of Cd-, Mn- or Ni-Doped ZnO Nanocrystals. The synthetic and purification procedures that generate Cd-, Mn- or Ni-doped ZnO nanocrystals were similar to those used to obtain the Mg-doped ZnO nanocrystals, except that designated amounts of $Cd(Ac)_2 \cdot 2H_2O$, $Mn(Ac)_2$ and $Ni(St)_2$ were employed as the dopant precursors, respectively.

In order to avoid redundancy, details of some reactions in this report shall be narrated in the related sections of main text or figure legends.

TEM Characterizations. Survey TEMs were conducted using a JEOL JEM 1230 transmission electron microscope operated at 80 kV and a Philips CM 200 microscope operated at 160 kV. High-resolution TEM (HRTEM) and energy-dispersive X-ray spectroscopy (EDX) were performed on a FEI TECNAI G^2 F20 transmission electron microscope operated at 200 kV. Samples for TEM analyses were prepared by dropping a dilute solution of nanocrystals onto ultrathin carbon-coated copper grids.

Scanning Transmission Electron Microscopy (STEM). High-angle annular dark-field STEM (HAADF-STEM) and line-scan EDX experiments were performed on a TECNAI G^2 F20 transmission electron microscope operated at an acceleration voltage of 200 kV equipped with an EDX/STEM HAADF detector. The dark-field micrographs were processed using TIA software (TECNAI imaging and analysis software).

Powder X-ray Diffraction (XRD). X-ray diffraction measurements were performed on a Bede D1 system operated at 20 kV and 30 mA with Cu Kα radiation ($\lambda = 1.5406$ Å). The data were collected with a step size of 0.01° and a counting time of 5 s per step in the 2θ range from 30° to 70°. XRD samples were prepared by dropping concentrated chloroform solutions of purified nanocrystals onto glass substrates. The samples were allowed to dry and then measured in reflection geometry.

Optical Measurements. UV−vis absorption experiments were performed on a UNICO UV-2102 ultraviolet−visible spectrophotometer equipped with a deuterium lamp and a tungsten-halogen lamp. PL spectra were recorded on an Edinburgh Instruments FLS-920 fluorescence spectrophotometer with a xenon lamp excited at 300 nm. Fourier transform infrared (FTIR) spectra were obtained on a Bruker Vector 22 spectrophotometer. The specimens for FTIR measurements were prepared by directly spotting hot aliquots from a reaction mixture which were sampled at different times during the reaction onto KBr crystal substrates.

Inductively Coupled Plasma Atomic Absorption Spectroscopy (ICP-AAS). ICP-AAS measurements were carried out using a Thermo Electron SOLAAR M6 atomic absorption spectrometer after digesting the purified nanocrystal samples in concentrated nitric acid (a 63% HNO_3 solution) for the elemental analyses of Zn and Mg.

X-ray Photoelectron Spectroscopy (XPS). XPS spectra were recorded on a Thermo ESCALAB-250 spectrometer using a monochromatic Al Kα radiation source (1486.6 eV). XPS samples were prepared by dropping concentrated chloroform solutions of purified nanocrystals onto silicon wafers. Note that for the XPS and ICP-AAS elemental analyses, the solutions of purified nanocrystals were filtered through 0.20 μm PTFE filters.

Results and Discussion

Choice of the Doped Nanocrystal System. We choose to study the Mg-doped ZnO nanocrystal system for several reasons. ZnO is a technologically important and environmentally friendly wide bandgap semiconductor with many unique properties.[39] Several types of devices based on ZnO nanocrystals, including field effect transistors,[40] photodetectors,[41] and solar cells[42] have been developed, revealing potential applications of ZnO nanocrystals for solution-processable electronics. Mg^{2+} ions are readily incorporated into the ZnO lattices by substitution, because the radius of Mg^{2+} (0.72 Å) is close to that of Zn^{2+} (0.74 Å). Studies on Mg-doped ZnO thin films with wurtzite (WZ) structure indicate that the bandgap of the film can be continuously tuned from 3.3 to 4.0 eV by adjusting Mg content.[43] A number of Mg-doped ZnO nanostructures, such as nanorods, have been fabricated.[44−47] Thus, doping ZnO nanocrystals with Mg is expected to be straightforward for generating nanocrystals with tunable optoelectronic properties, which are promising for use in solution-processable devices.

The synthesis of the Mg-doped ZnO nanocrystals offers an ideal system to explore the effects of Mg dopants on the growth of the doped nanocrystals. As described in the Experimental Section, the reactions to obtain the doped nanocrystals, inspired

(39) Ozgur, U.; Alivov, Y. I.; Liu, C.; Teke, A.; Reshchikov, M. A.; Dogan, S.; Avrutin, V.; Cho, S. J.; Morkoc, H. *J. Appl. Phys.* **2005**, *98*, 041301.
(40) Sun, B. Q.; Sirringhaus, H. *Nano Lett.* **2005**, *5*, 2408–2413.
(41) Jin, Y. Z.; Wang, J. P.; Sun, B. Q.; Blakesley, J. C.; Greenham, N. C. *Nano Lett.* **2008**, *8*, 1649–1653.
(42) Beek, W. J. E.; Wienk, M. M.; Janssen, R. A. J. *Adv. Mater.* **2004**, *16*, 1009–1013.
(43) Ohtomo, A.; Kawasaki, M.; Koida, T.; Masubuchi, K.; Koinuma, H.; Sakurai, Y.; Yoshida, Y.; Yasuda, T.; Segawa, Y. *Appl. Phys. Lett.* **1998**, *72*, 2466–2468.
(44) Park, W. I.; Yi, G. C.; Kim, M. Y.; Pennycook, S. J. *Adv. Mater.* **2003**, *15*, 526–529.
(45) Hsu, H. C.; Wu, C. Y.; Cheng, H. M.; Hsieh, W. F. *Appl. Phys. Lett.* **2006**, *89*, 013101.
(46) Lin, S. S.; Hong, J. I.; Song, J. H.; Zhu, Y.; He, H. P.; Xu, Z.; Wei, Y. G.; Ding, Y.; Snyder, R. L.; Wang, Z. L. *Nano Lett.* **2009**, *9*, 3877–3882.
(47) Lorenz, M.; Kaidashev, E. M.; Rahm, A.; Nobis, T.; Lenzner, J.; Wagner, G.; Spemann, D.; Hochmuth, H.; Grundmann, M. *Appl. Phys. Lett.* **2005**, *86*, 143113.

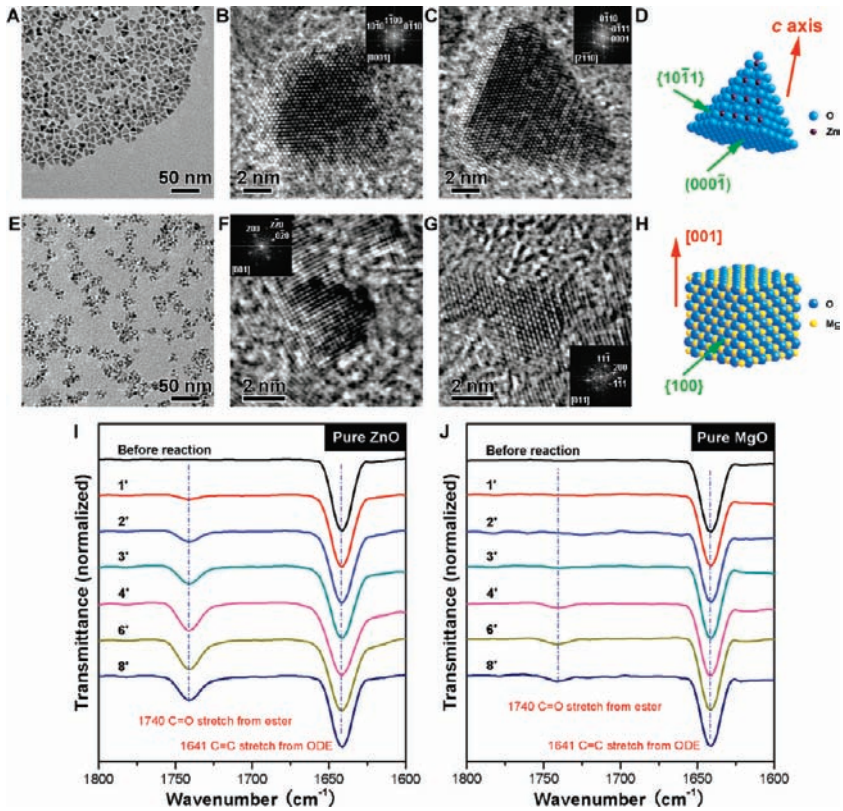

Figure 1. Pure ZnO and MgO nanocrystals. (A) A typical TEM image of pure ZnO nanocrystals. (B) and (C) HRTEM images of two pure ZnO nanocrystals viewed along the [0001] and [2−1−10] zone axes, respectively. Insets are the corresponding fast Fourier transform (FFT) patterns. (D) A three-dimensional structural model (not to scale) showing the wurtzite (WZ) structure of pure ZnO nanocrystals. (E) Typical TEM image of pure MgO nanocrystals. (F) and (G) HRTEM images of two pure MgO nanocrystals viewed along the [001] and [011] zone axes, respectively. Insets are the corresponding FFT patterns. (H) Three-dimensional structural model (not to scale) showing the rock-salt structure of pure MgO nanocrystals. (I) and (J) Temporal evolution of FTIR spectra recorded from the reactions for the formation of pure ZnO and MgO nanocrystals, respectively. All spectra are normalized to the relatively intense C═C vibration band at 1641 cm^{-1} originating from ODE (the solvent) as the standard.

by the protocol to grow pure ZnO nanocrystals,[48] involve alcoholysis of metal carboxylate salts without use of any additional surfactants. The chemical reactions leading to the metal oxide have been well addressed by previous works.[48,49] Such a simple and well-developed synthetic strategy facilitates experimental design in the present study, which focuses on the effects of introduction of dopants. In addition, the method used in our study has been proved to be successful for preparing many oxide nanocrystals with high yields.[48,50,51] Therefore, insights revealed on the basis of the Mg-doped ZnO nanocrystals are expected to be applicable to other oxide nanocrystal systems. Another advantage of our synthetic scheme is that, from a green chemistry point of view, the chemicals used (such as metal fatty acid salts, alcohols, and ODE) are nontoxic, air stable and inexpensive.

Pure ZnO and MgO Nanocrystals. The syntheses of pure ZnO and MgO nanocrystals provide an essential basis for the fabrication of doped nanocrystals. Pure ZnO nanocrystals were obtained by injecting alcohol into a solution of $Zn(St)_2$. Figure 1A shows that the reaction generates faceted ZnO nanoparticles, 10−15 nm in dimension. HRTEM analyses (Figure 1, B−D and Figure S1 (Supporting Information)) reveal that the crystal structure of these faceted nanoparticles fits that of WZ type of ZnO. Pure MgO nanocrystals were also obtained under similar conditions except that $Mg(St)_2$ was employed as the metal precursor. TEM investigations (Figure 1E) show that the pure MgO nanocrystals exhibit irregular shapes and are often found to be attached to each other, forming nanoflowers. HRTEM analyses (Figure 1F−H) imply that the MgO nanocrystals have cubic rock-salt structure identical to that of bulk MgO.

Both reactions were monitored by recording FTIR spectra of the aliquots withdrawn from the reaction flasks. As shown in Figure 1, I and J, the vibration peak at 1740 cm^{-1} is assigned as C═O stretch from ester. This indicates that the side product of the alcoholysis reactions is ester, consistent with the study by Peng and co-workers.[48] Thus, the vibration peak at 1740 cm^{-1} can be served as a semiquantitative probe for monitoring formation of oxide nanocrystals. Comparing the temporal evolution of the FTIR spectra shown in Figure 1, I and J, the intensities of the ester peaks in Figure 1J are lower than those of the corresponding spectra in Figure 1I. This fact suggests that the reactivity of the Zn precursor, $Zn(St)_2$, is higher than that of the Mg precursor, $Mg(St)_2$.

The relatively higher reactivity of $Zn(St)_2$ facilities to generate Mg-doped ZnO nanocrystals that only have crystallographic structures identical to those of ZnO. As shown in the next subsection, in the 50% $Mg(St)_2$ reaction in which 0.5 mmol of $Mg(St)_2$ and 0.5 mmol of $Zn(St)_2$ are used as starting materials, high-quality Mg-doped ZnO nanocrystals with WZ structure are

(48) Chen, Y. F.; Kim, M.; Lian, G.; Johnson, M. B.; Peng, X. G. *J. Am. Chem. Soc.* **2005**, *127*, 13331–13337.
(49) Clavel, G.; Willinger, M. G.; Zitoun, D.; Pinna, N. *Adv. Funct. Mater.* **2007**, *17*, 3159–3169.
(50) Pinna, N.; Niederberger, M. *Angew. Chem., Int. Ed.* **2008**, *47*, 5292–5304.
(51) Jana, N. R.; Chen, Y. F.; Peng, X. G. *Chem. Mater.* **2004**, *16*, 3931–3935.

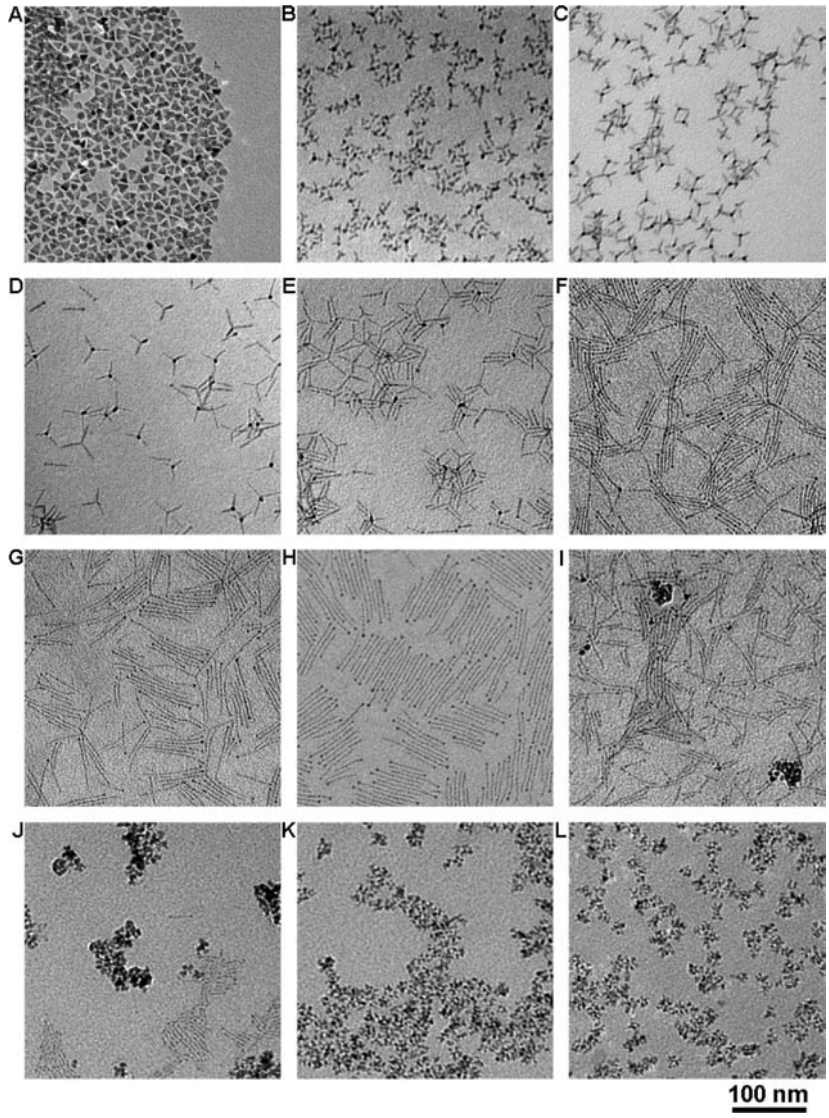

Figure 2. Shape evolution of the nanocrystals from the reactions with different molar ratios of $Mg(St)_2$ in the reagents. (A−L) Typical TEM images of the nanocrystals from the 0%, 2%, 5%, 10%, 20%, 30%, 40%, 50%, 60%, 70%, 80%, and 100% $Mg(St)_2$ reactions, respectively.

obtained without formation of nanocrystals with cubic structure identical to that of MgO. In contrast, in another study aiming to synthesize indium-doped ZnO nanocrystals which also employed the alcoholysis approach, although a much lower relative concentration, 5 mol %, of the indium precursor was used, formation of individual nanocrystals with cubic structure identical to that of indium oxide was found to be inevitable. This is owing to the relatively higher reactivity of the indium precursor than that of the Zn precursor, $Zn(St)_2$.[52]

Shape Evolution of the Doped Nanocrystals. Sets of reactions with different molar ratios of $Mg(St)_2$ in the reagents were conducted to systematically study the doping effects on the resulting nanocrystals. As shown in Figure 2 and Figure S2 (Supporting Information), the shape evolution of the doped nanocrystals is evident.

Tetrapods from the 5% $Mg(St)_2$ reaction and ultrathin nanowires from the 50% $Mg(St)_2$ reaction are selected as two typical examples, which are highlighted in Figure 3, to illustrate the dopant-induced shape evolution of the Mg-doped ZnO

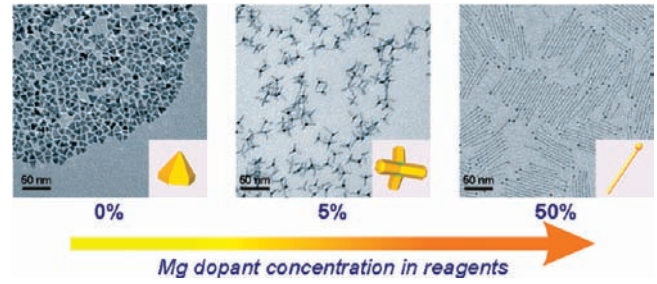

Figure 3. Representative TEM images of the nanocrystals from the 0%, 5% and 50% $Mg(St)_2$ reactions, emphasizing the shape evolution of colloidal nanocrystals due to the increasing Mg dopant concentrations in the reagents (highlighted by the arrow). Insets are the corresponding three-dimensional models of the nanocrystals (not to scale).

nanocrystals. Detailed HRTEM analyses were conducted on the tetrapods and the ultrathin nanowires. As shown in Figure 4, A and B, the WZ arms of the tetrapods, 3.6 ± 0.3 nm in diameters, are found to grow along the [0001] direction (see additional data in Figure S3 (Supporting Information)). Due to the presence of arms that hinder most central regions of the tetrapods, in direct imaging of the tetrapods it is difficult to obtain atomic

(52) Wang, Q. L.; Yang, Y. F.; He, H. P.; Chen, D. D.; Ye, Z. Z.; Jin, Y. Z. *Nanoscale Res. Lett.* **2010**, *5*, 882–888.

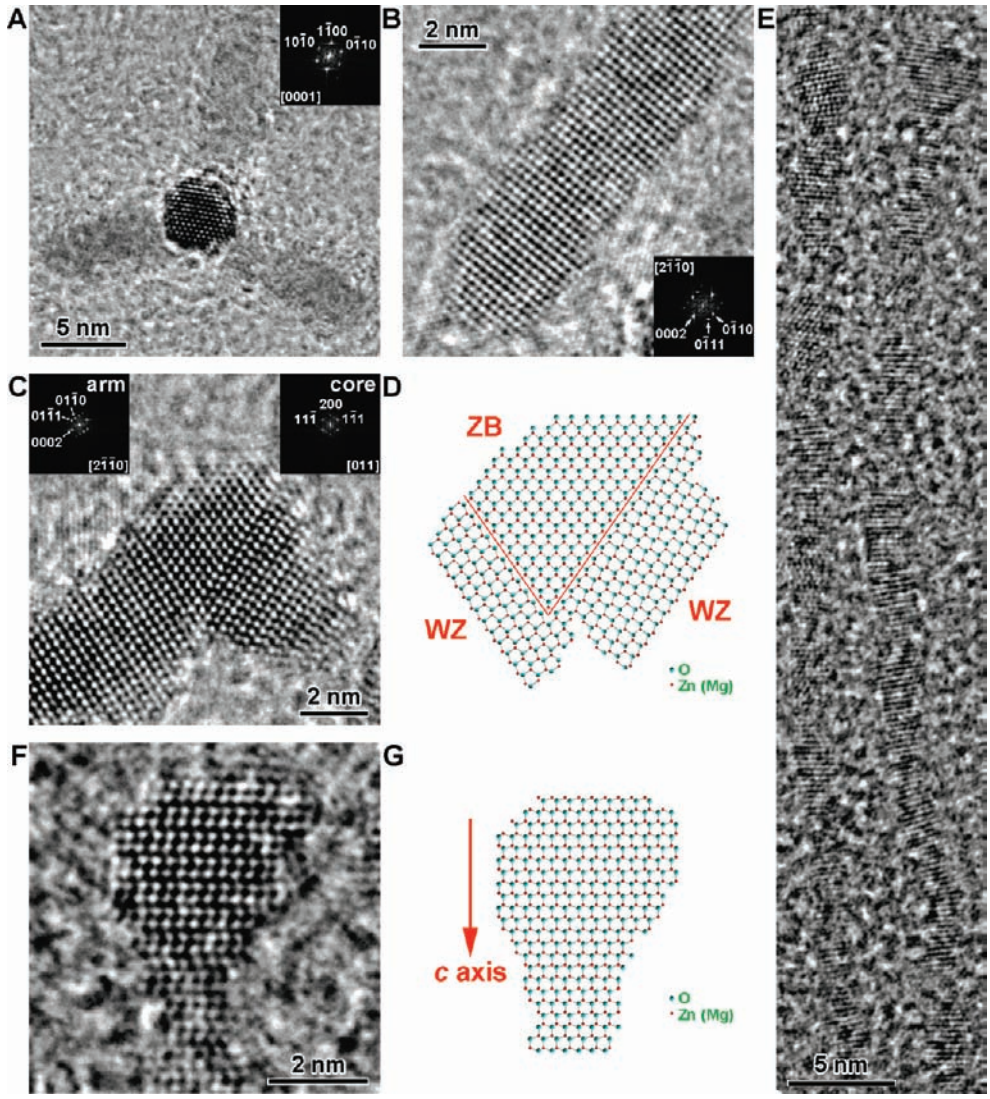

Figure 4. HRTEM analyses on the tetrapods from the 5% $Mg(St)_2$ reaction and the ultrathin nanowires from the 50% $Mg(St)_2$ reaction. (A, B) HRTEM images of two tetrapod arms viewed from different directions, which illustrate the WZ structure of the arms. Insets are the corresponding FFT patterns. (C, D) HRTEM image of the central region of a bipod and the corresponding two-dimensional atomic simulation, respectively. Insets are the FFT patterns from the arm region (top left) and the core region (top right). (E) A HRTEM image of two ultrathin nanowires with WZ structure, which grow along the *c*-axis directions. (F, G) HRTEM image of the head area of a tadpolelike ultrathin nanowire and the corresponding two-dimensional atomic simulation, respectively.

resolution images that fully uncover crystalline features of the core area (Figure S4, Supporting Information). Thus, we choose to image the bipods or tripods that are tetrapods with one or two arms missing. Results (see Figure 4C and Figure S5 (Supporting Information)) show that the tetrapods match the polytypism model:[53] the {0002} facets of the WZ arms are epitaxially grown from the atomically identical {111} facets of the zincblende (ZB) cores (Figure 4D). Regarding the ultrathin nanowires from the 50% $Mg(St)_2$ reaction, TEM observations (Figure 2H and Figure S6 (Supporting Information)) illustrate that the ultrathin nanowires are fairly flexible and exhibit a tadpolelike morphology: a spherical particle, ~3.0 nm in diameter, is attached to one end of each wire. The nanowires are 64.6 ± 17.6 nm in length and 1.4 ± 0.2 nm in diameter with aspect ratios generally greater than 30. HRTEM images (Figure 4,E−G and Figures S7 and S8 (Supporting Information)) suggest that the single crystalline wires with WZ structure are continuously grown from the WZ heads by sharing *c*-axis directions. ICP-AAS measurements (see Table S1 (Supporting Information)), which are supported by EDX and XPS examinations on selected samples (Figures S3, S6 and S9 (Supporting Information)), reveal that the Mg concentrations of the tetrapods and the ultrathin nanowires are ~3.0 atom % and 22.6 atom %, respectively.

It is of interest to reveal the distribution of dopants in the Mg-doped ZnO nanocrystals. STEM and line-scan EDX analyses (Figure S10, Supporting Information) on a number of tetrapods and ultrathin nanowires indicate no segregation of Mg-rich domains within the nanocrystals. Nevertheless, it is challenging to acquire line-scan EDX spectra with high statistics due to the low Mg concentration of the tetrapods, the small dimension of the nanowires, beam damage by prolonged high-energy electron illumination, specimen drift, and hydrocarbon contamination of the specimen and sample holder. Here we adopted a quantitative etching procedure, which was developed for determining the radial distribution of the elements in core/

(53) Manna, L.; Milliron, D. J.; Meisel, A.; Scher, E. C.; Alivisatos, A. P. *Nat. Mater.* **2003**, *2*, 382–385.

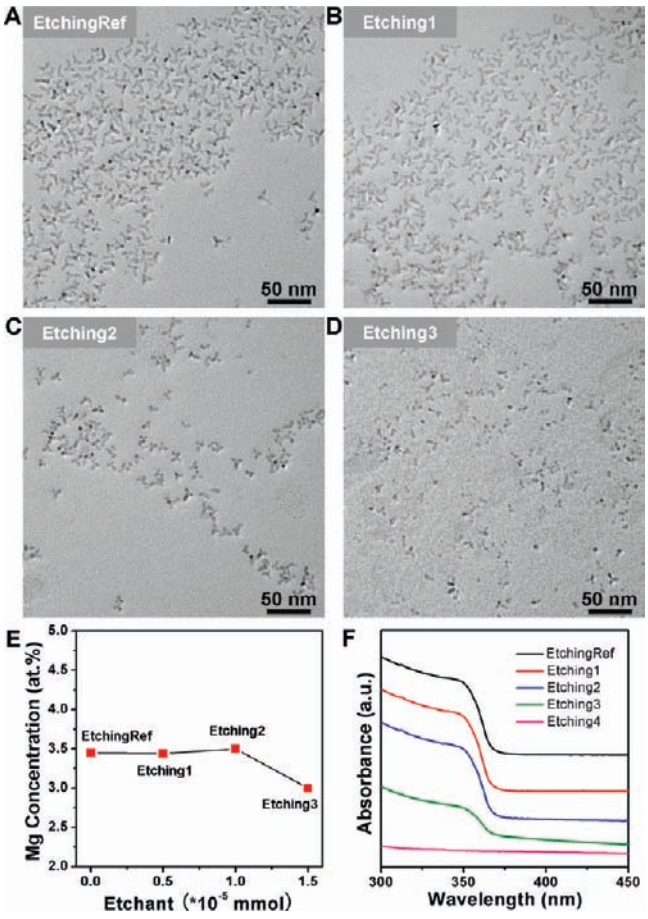

Figure 5. (A−D) Typical TEM images for the original tetrapods and the etched nanocrystals from the quantitative etching experiments (see Figure S11 and Table S2 in Supporting Information for more experimental details). (E) Mg concentrations of the purified etched nanocrystals, which are determined by ICP-AAS, as a function of the amounts of the etchant. (F) UV−vis spectra of the solutions from the quantitative etching experiments.

shell nanocrystals,[54,55] to support our view that no segregation of Mg-rich domains was present within the doped nanocrystals. To do so, a series of etchant solutions with different concentrations of trifluoroacetic acid were mixed with solutions containing equal amounts of doped nanocrystals (see Figure S11 and Table S2 for details, Supporting Information). TEM observations (Figure 5, A−D) on the samples of etched tetrapods indicate that, upon etching, the lengths of the tetrapod arms were continuously decreased. The solutions of etched tetrapods were purified by multiple methanol extraction to remove species containing the ions etched away from the oxide nanocrystals and the residuals of the etchant. ICP-AAS measurements (Figure 5E) on the etched tetrapods after purification indicate that the Mg concentrations are in the range of 3.0−3.5 atom %. The invariable dopant concentrations are reflected by the identical optical absorbance features of the etched nanocrystals (Figure 5F) since the incorporation of Mg dopants shall modify the optical properties of the nanocrystals (see more discussion later). With these results, we assumed a reasonable homogeneous distribution of Mg dopants in the nanocrystals. Recently Lauhon et al. developed a powerful method by employing atom probe tomography and quantitative tomographic reconstruction techniques to study dopant distribution in an individual nanowire grown by vapor−liquid−solid (VLS) strategy.[56] It is highly desirable to apply such a method to study solution-grown colloidal doped nanocrystals.

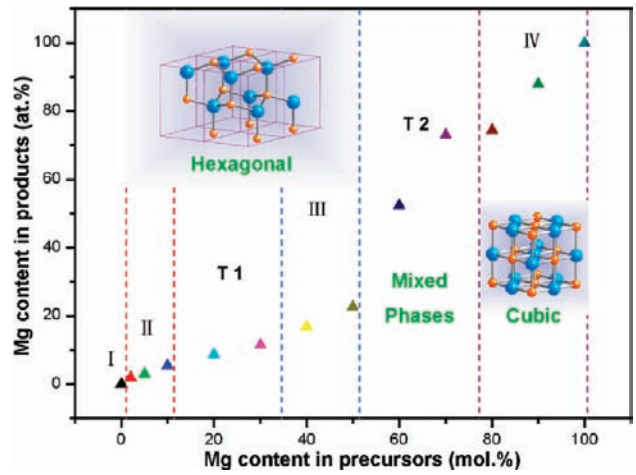

Figure 6. Mg concentrations of the nanocrystals, determined by ICP-AAS, as a function of the relative concentrations of $Mg(St)_2$ in the reagents. Regions I, II, III and IV represent the nanocrystals with typical morphologies of faceted particles, tetrapods, ultrathin nanowires and irregular particles, respectively. Regions T1 and T2 correspond to two shape transition zones.

The shape evolutions (Figure 2) and the structural features and chemical compositions of the doped nanocrystals are summarized in Figure 6, which are supported by XRD, ICP-AAS, XPS, HRTEM and EDX measurements on a variety of samples. Region I represents the faceted nanoparticles of pure ZnO. In region II, a small amount of the Mg precursor, as low as 2 mol % of $Mg(St)_2$ in the starting materials, significantly changes the morphology of the resulting nanocrystals, leading to tetrapods. The tetrapod-shaped nanocrystals are also obtained in the products from the 5% and 10% $Mg(St)_2$ reactions. For the 2%, 5% and 10% $Mg(St)_2$ reactions, the 5% $Mg(St)_2$ reaction has a maximum yield, as high as over 95%, of quality tetrapods which are highly uniform in terms of crystal dimensions. Region T1 corresponds to a shape transition zone from tetrapods to ultrathin nanowires. The 20% $Mg(St)_2$ reaction yields a majority of tetrapods accompanied by a fraction of tripods, bipods and wires, while the 30% $Mg(St)_2$ reaction yields mostly nanowires together with a small amount of bipods, tripods and tetrapods. HRTEM investigations on the products from the 20% $Mg(St)_2$ reaction (see Figure S12, Supporting Information) suggest that both branched nanocrystals with ZB cores and tadpolelike nanowires with WZ heads are observed. Region III is associated with the 40% and 50% $Mg(St)_2$ reactions, in which the ultrathin nanowires dominate in the products. For regions I, II, T1 and III, XRD profiles of the nanocrystals from the 0%, 2%, 5%, 10%, 20%, 30%, 40% and 50% $Mg(St)_2$ reactions, as shown in Figure 7A, exhibit typical size-broadened reflections from WZ-type of ZnO, in agreement with the HRTEM studies. ICP-AAS measurements show an approximately linear scaling of Mg concentration in the nanocrystals with the molar ratio of $Mg(St)_2$ in the reagents when it is in the range of 0−20 mol % (Figure 6). For the 40% and 50% $Mg(St)_2$ reactions, the Mg concentra-

(54) Battaglia, D.; Blackman, B.; Peng, X. *J. Am. Chem. Soc.* **2005**, *127*, 10889–10897.
(55) Chen, D.; Zhao, F.; Qi, H.; Rutherford, M.; Peng, X. *Chem. Mater.* **2010**, *22*, 1437–1444.
(56) Perea, D. E.; Hernesath, E. R.; Schwalbach, E. J.; Lensch-Falk, J. L.; Voorhees, P. W.; Lauhon, L. J. *Nat. Nanotechnol.* **2009**, *4*, 315–319.

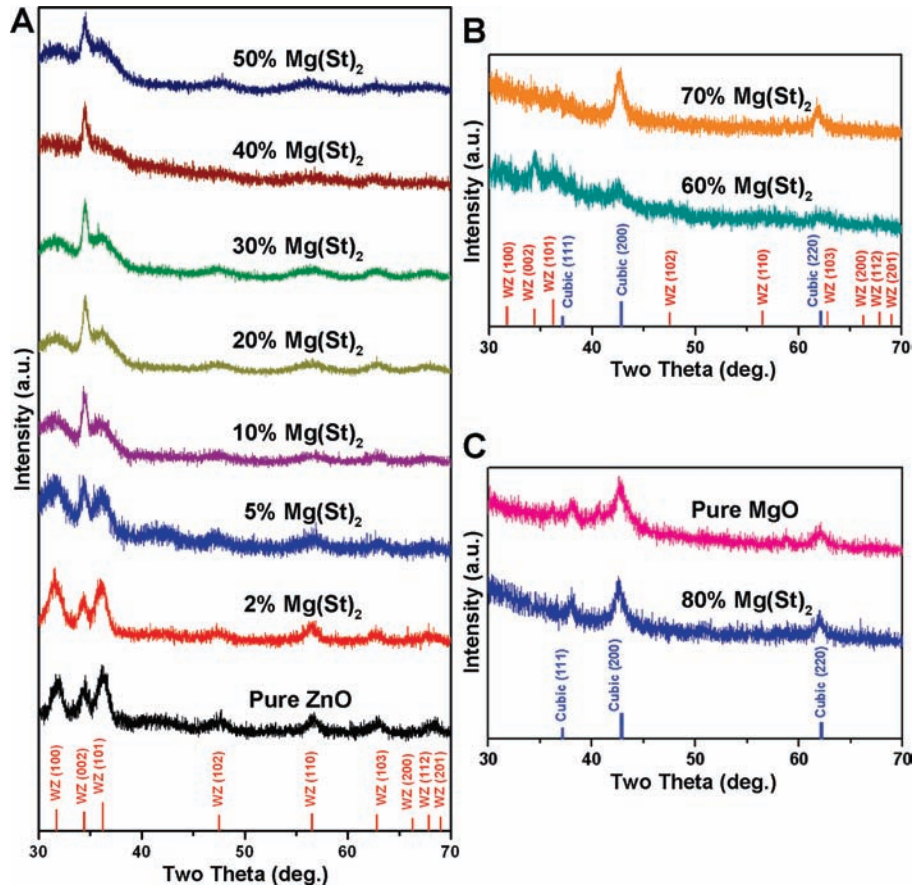

Figure 7. XRD profiles of the nanocrystals from the reactions with different molar ratios of $Mg(St)_2$ in the reagents. The red and blue lines (bottom) represent the diffraction peaks of bulk ZnO (WZ) and MgO (cubic), respectively. (A) The nanocrystals from the 0%, 2%, 5%, 10%, 20%, 30%, 40%, and 50% $Mg(St)_2$ reactions having WZ structure. (B) The nanocrystals from the 60% and 70% $Mg(St)_2$ reactions, with the presence of both WZ and cubic structures. (C) The nanocrystals from the 80% and 100% $Mg(St)_2$ reactions having cubic structure.

tion in the nanocrystals reaches a limit of ~22.6 atom %. Together with the TEM observations (Figure 2, A−H), a clear trend is that, the higher the Mg concentration in the nanocrystals, the longer the lengths and the smaller the diameters of the tetrapod arms or the nanowires. In other words, anisotropy of the tetrapod arms or the nanowires correlates to the Mg concentration in the products which is determined by the molar ratio of $Mg(St)_2$ in the starting materials. This is confirmed by the fact that the (002) diffraction peaks in the corresponding XRD profiles (Figure 7A), which are associated with the preferential growth direction, have strongly sharpened up along with the increasing molar ratios of $Mg(St)_2$ in the reagents.

Similar to region T1, region T2 corresponds to another shape transition zone from ultrathin nanowires to irregular particles. The product from the 60% $Mg(St)_2$ reaction contains more nanowires, relative to the product from the 70% $Mg(St)_2$ reaction, which yields mostly irregular particles. Regarding region IV, only irregular nanoparticles are observed. XRD and HRTEM analyses (Figure 7C and Figure S13 (Supporting Information)) indicate that crystal structures of the irregular nanoparticles from the 80%, 90% and 100% $Mg(St)_2$ reactions are similar to that of bulk MgO.

To conclude, different relative concentrations of $Mg(St)_2$ in the starting materials lead to nanocrystals exhibiting dramatic morphological, structural and compositional changes. When the relative concentration of the Mg precursor in the reagents is less than 50 mol % (regions I, II, III and T1), Mg-doped ZnO nanocrystals that adopt the ZnO lattices are obtained. The shape evolution of the Mg-doped ZnO nanocrystals with increasing relative concentrations of the Mg precursor follows the order from the faceted particles (region I) to the tetrapods (region II) and then to the ultrathin nanowires (region III), which are depicted in Figure 3. Further increase of the molar ratios of $Mg(St)_2$ in the reagents results in phase transition of the resulting nanocrystals from the hexagonal phase (regions I, II, III and T1) to mixed phases (region T2) and then to the cubic phase (region IV).

Optical Properties of the Mg-Doped ZnO Nanocrystals. The incorporation of Mg^{2+} ions into the ZnO lattices significantly modifies the optoelectronic properties of the nanocrystals. The optical bandgap of the doped nanocrystals can be continuously tuned from 3.3 to 3.9 eV, as revealed by the UV−vis absorption spectra (Figure 8, left and Figure S14A (Supporting Information)). Regarding the PL spectra of the Mg-doped ZnO nanocrystals, a continuous blue shift of the near band edge (NBE) emission from 382 to 328 nm is observed (Figure 8, right and Figure S14B (Supporting Information)). Note that quantum confinement effect (QCE) is present in some samples of ultrathin nanowires (because of the very small diameters of the nanowires which are close to the exciton Bohr radius of bulk ZnO, 1.8 nm) and contributes to the blue-shift. The bandgap bowing fit to the data is not available due to the presence of QCE. Nevertheless, a precise determination of QCE is difficult and beyond the scope of this study. For a rough estimation, according

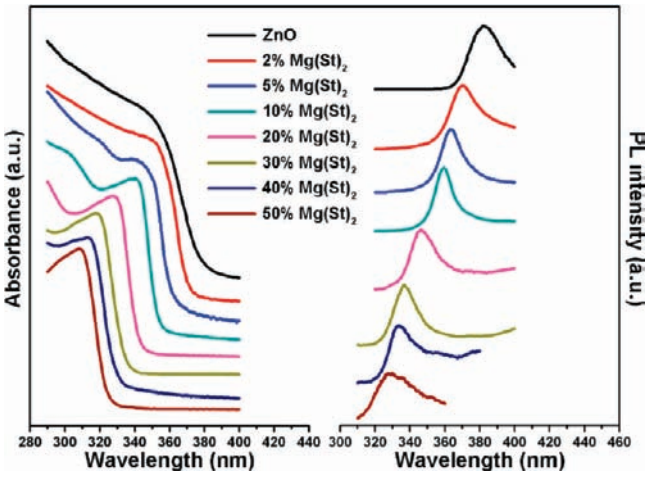

Figure 8. Tunable optical properties of the Mg-doped ZnO nanocrystals. Room temperature optical absorption (left) and photoluminescence (right) spectra in UV-region of the nanocrystals from the 0%, 2%, 5%, 10%, 20%, 30%, 40% and 50% $Mg(St)_2$ reactions.

to the model developed by Gu et al.,[57] the QCE-induced blue-shift in the case of the ultrathin nanowires (1.4 nm in diameter) is ~0.15 eV, which is significantly smaller than the observed bandgap variation. This indicates a strong bandgap bowing due to Mg doping. In addition, the conversion of the intensity ratio of NBE to green emission when the molar ratio of $Mg(St)_2$ in the reagents exceeds 10 mol %, as illustrated by Figure S14B (Supporting Information), reflects elevated Mg concentrations in the doped nanocrystals, which induce more defects.

Achieving doped ZnO nanocrystals with desired shapes in conjunction with the ability of tailoring optoelectronic properties is attractive and exciting for employing these materials for various applications. For instance, the Mg-doped ZnO tetrapods may be promising for hybrid nanocrystal/polymer solar cell applications because of both improved charge transport due to their three-dimensional nature[58] and increased open circuit voltage induced by Mg doping.[59] Solution-processable UV photodetectors with shorter cutoff wavelength might be fabricated by using ultrathin nanowire films as active layers which possess very large surface area, readily facilitating gas adsorption and desorption from the nanocrystal surfaces,[41] thereby ensuring prompt transformations of the surface trapping states and improving device performances.

Initial Growth Seeds of the Tetrapods and the Ultrathin Nanowires. To understand the underlying mechanism of the observed shape evolution of the Mg-doped ZnO nanocrystals, the critical issue that governs the formation of the doped nanocrystals with defined morphologies, i.e. tetrapods and ultrathin nanowires, must be explored. Shape control of undoped nanocrystals has been extensively studied in literature.[5,7,8,14,60−63] For the kinetically driven shape controlled growth of nanocrystals, crystallographic phase of growth seeds and surface ligands that modulate surface energy of growing crystallites by selective adhesion are two important factors.[8] Therefore the growth seeds and the surface ligands for the Mg-doped ZnO nanocrystals were characterized and discussed in detail, which provide insights for the growth mechanism of the doped nanocrystals. This subsection discusses the issues of growth seeds for the doped ZnO nanocrystals. Identification of the surface ligands and impacts of the ligands on the formation of oxide nanocrystals shall be discussed later in the text.

Tracking the growth processes of the doped nanocrystals may shed light on the formation of the growth seeds. Thus the 5% and 50% $Mg(St)_2$ reactions, which resulted in quality samples of the tetrapods and the ultrathin nanowires, respectively, were monitored by UV−vis absorption spectra which allowed detection of nanocrystals in the reaction solutions. As shown in Figure 9A and D, UV−vis absorbance signals were observed after 2.5−3 min for the 5% $Mg(St)_2$ reaction and 3.5−4 min for the 50% $Mg(St)_2$ reaction, respectively. In this work we define the nanocrystals in the first aliquots that generate absorbance peaks as the initial growth seeds of the resulting doped nanocrystals. The slightly red shifts of the absorbance peaks in the temporal evolution of UV−vis spectra (Figure S15 (Supporting Information)) for both reactions reflect the growth of the nanocrystals in the reaction solutions. As suggested by one of the reviewers, time-dependent PL technique, which is widely used to study the growth and ripening of fluorescent nanocrystals, such as CdSe quantum dots,[64,65] may provide more information on the growth and ripening of the doped nanocrystals and shall be conducted in future experiments.

After purification by successive extractions with methanol/hexane, the initial growth seeds of the doped nanocrystals were characterized by TEM. As shown in Figure 9, B and C, for the 5% $Mg(St)_2$ reaction, the majority of the initial growth seeds are bipods and tripods with ZB cores. For the 50% $Mg(St)_2$ reaction, the growth seeds are short tadpolelike nanowires, 5−20 nm in length, with WZ heads (Figure 9E and F). ICP-AAS measurements on the initial growth seeds which were further purified to remove any residual metal salt precursors show that the Mg concentrations of the growth seeds from the 5% and 50% $Mg(St)_2$ reactions are ~2.5 atom % and 20.0 atom %, respectively. This implies the incorporation of Mg^{2+} ions into the initial growth seeds at the primary growth stages.

TEM observations on samples of purified nanocrystals obtained from the aliquots of the 5% $Mg(St)_2$ reaction indicate that the initial growth seeds with ZB cores gradually develop and form quality tetrapods with uniform dimensions (Figure S16, A−C, Supporting Information). Similar experiments show that the initial growth seeds in the 50% $Mg(St)_2$ reaction, the short tadpolelike nanowires elongate along the *c*-axis of WZ structure and ultrathin nanowires are obtained (Figure S16, D−F (Supporting Information)).

The growth processes of the doped nanocrystals, as monitored by UV−vis absorption and TEM techniques, indicate that the creation of the doped nanocrystals with different shapes is attributed to the formation of initial growth seeds with different crystallographic structures at the primary growth stages. We further suggest that different crystal structures of the initial growth seeds is due to the relative concentrations of the Mg

(57) Gu, Y.; Kuskovsky, I. L.; Yin, M.; O'Brien, S.; Neumark, G. F. *Appl. Phys. Lett.* **2004**, *85*, 3833–3835.
(58) Sun, B. Q.; Marx, E.; Greenham, N. C. *Nano Lett.* **2003**, *3*, 961–963.
(59) Olson, D. C.; Shaheen, S. E.; White, M. S.; Mitchell, W. J.; van Hest, M.; Collins, R. T.; Ginley, D. S. *Adv. Funct. Mater.* **2007**, *17*, 264–269.
(60) Asokan, S.; Krueger, K. M.; Colvin, V. L.; Wong, M. S. *Small* **2007**, *3*, 1164–1169.
(61) Nair, P. S.; Fritz, K. P.; Scholes, G. D. *Small* **2007**, *3*, 481–487.
(62) Wang, W.; Banerjee, S.; Jia, S. G.; Steigerwald, M. L.; Herman, I. P. *Chem. Mater.* **2007**, *19*, 2573–2580.
(63) Hickey, S. G.; Waurisch, C.; Rellinghaus, B.; Eychmuller, A. *J. Am. Chem. Soc.* **2008**, *130*, 14978–14981.
(64) Thessing, J.; Qian, J. H.; Chen, H. Y.; Pradhan, N.; Peng, X. G. *J. Am. Chem. Soc.* **2007**, *129*, 2736–2737.
(65) de Mello Donegá, C.; Hickey, S. G.; Wuister, S. F.; Vanmaekelbergh, D.; Meijerink, A. *J. Phys. Chem. B* **2002**, *107*, 489–496.

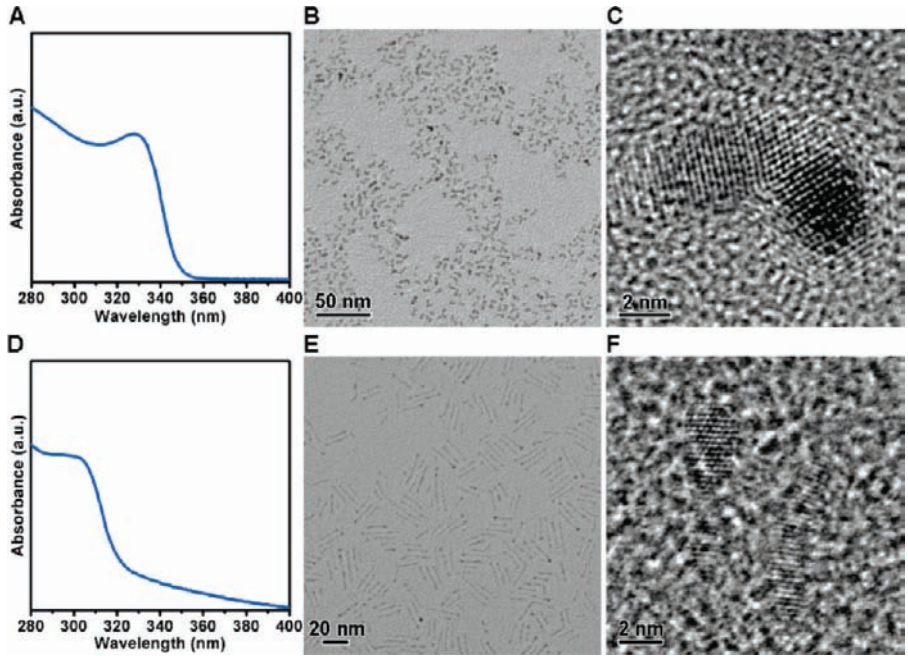

Figure 9. Initial growth seeds from the 5% and 50% $Mg(St)_2$ reactions. (A) A typical UV−vis spectrum, (B) a typical TEM image and (C) a HRTEM image of the initial growth seeds from the 5% $Mg(St)_2$ reaction, suggesting the formation of bipods or tripods with ZB cores. (D) A typical UV−vis spectrum, (E) a typical TEM image and (F) a HRTEM image of the initial growth seeds from the 50% $Mg(St)_2$ reaction, revealing that the initial growth seeds from the 50% $Mg(St)_2$ reaction are short tadpolelike nanowires with WZ heads.

precursor in the reagents. This deduction is supported by the fact of incorporation of Mg^{2+} ions into the initial growth seeds. The Mg concentration of the initial growth seeds of the ultrathin nanowires is much higher than that of the initial growth seeds of the tetrapods, which is caused by a much higher relative concentration of the Mg precursor of the 50% $Mg(St)_2$ reaction than that of the 5% $Mg(St)_2$ reaction. In other words, for the 50% $Mg(St)_2$ reaction, an equal amount of $Zn(St)_2$ and $Mg(St)_2$ in the starting materials favors the formation of the initial growth seeds with WZ heads, which eventually leads to the ultrathin nanowires. We carried out a set of experiments in which the $Mg(St)_2$ molar ratios are kept as 50 mol % to test this hypothesis. Results show that all the reactions yield tadpolelike nanowires with WZ heads although the total cation quantity is varied from 0.5 to 2 mmol (Figure 10). Similarly, in another set of experiments in which the $Mg(St)_2$ molar ratios are kept as 5 mol % and the total cation quantity is varied from 0.75 to 1.5 mmol, tetrapod shaped nanocrystals are obtained in the products from all reactions (Figure S17 (Supporting Information)). With these results, we suggest that the relative concentration of the Mg precursor in the reagents, which affects the crystal structures of the initial growth seeds, is a decisive factor that governs the shapes of the doped nanocrystals in our reaction systems.

Seeded Growth of Tetrapods from Small ZnO Seeds. In this subsection, we focus on the doping effects of Mg^{2+} ions on the crystal structures of the host lattices at the primary growth stage. It is important because the formation of initial growth seeds, which are nanocrystals at the primary growth stages, with different crystallographic structures affects the morphologies of the doped nanocrystals. The initial growth seeds with ZB cores in the 5% $Mg(St)_2$ reaction are of particular interest since the ZB phase of ZnO or Mg-doped ZnO is generally unstable and only form under certain conditions.[66] Nevertheless, for the doping procedure discussed above, the formation of initial growth seeds is accompanied by the incorporation of Mg^{2+} ions into the host lattices, which makes such a study more or less difficult.

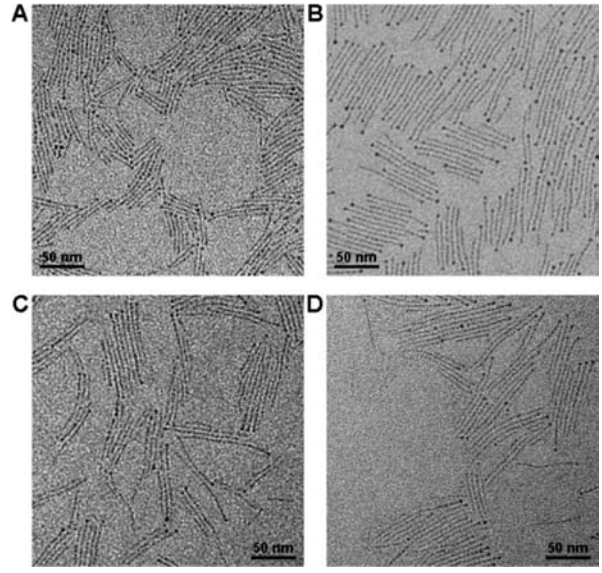

Figure 10. TEM images of ultrathin nanowires from a set of reactions in which the total quantity of metal precursors, with fixed $Mg(St)_2$:$Zn(St)_2$ ratio of 50:50 mol %, is varied from 0.5 to 2 mmol. (A) 0.25 mmol of $Zn(St)_2$ and 0.25 mmol of $Mg(St)_2$ were used as starting materials. (B) 0.5 mmol of $Zn(St)_2$ and 0.5 mmol of $Mg(St)_2$ were used as starting materials. (C) 0.75 mmol of $Zn(St)_2$ and 0.75 mmol of $Mg(St)_2$ were used as starting materials. (D) 1 mmol of $Zn(St)_2$ and 1 mmol of $Mg(St)_2$ were used as starting materials.

In this regard, we designed a seeded growth experiment, which decoupled the formation of growth seeds and the incorporation of Mg^{2+} ions into the host lattices, as depicted by Figure S18 (Supporting Information). A quantity of 0.5 mmol of pure $Zn(St)_2$ was reacted with alcohol for 4 min to generate

(66) Ashrafi, A.; Jagadish, C. *J. Appl. Phys.* **2007**, *102*, 071101.

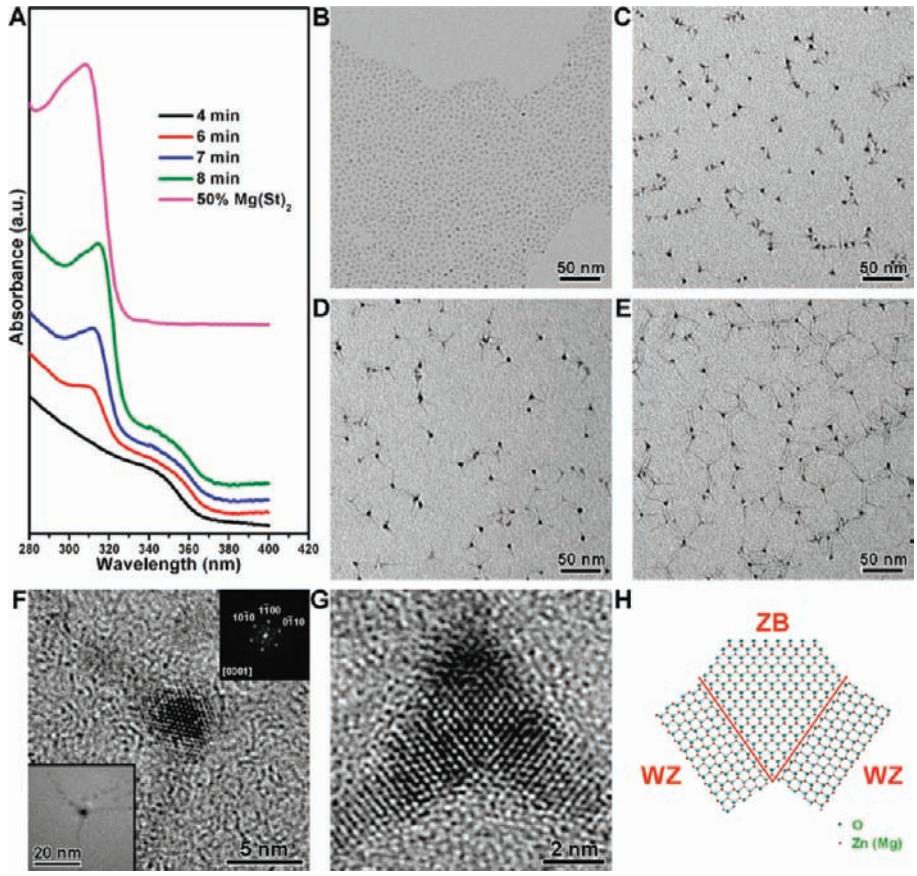

Figure 11. Seeded growth of tetrapods from small ZnO seeds. (A) Temporal evolution of UV−vis spectra of nanocrystals grown in the seeded growth experiment. The emergence of the peaks at ∼313 nm is attributed to the growth of the tetrapod arms, which exhibit UV−vis absorption features comparable to those of the ultrathin nanowires from the 50% $Mg(St)_2$ reaction, as indicated by the magenta line. (B−E) Temporal evolution of the morphologies of the nanocrystals. TEM images were recorded from the nanocrystals in the aliquots which were taken from the reaction flask at 4 min (before the injection of the $Mg(St)_2$ solution), 6, 7, and 8 min, respectively. (F) A HRTEM image of a tetrapod arm viewed from the [0001] direction. Insets are the corresponding low-magnification TEM images (bottom left) and FFT pattern (top right). (G) and (H) HRTEM image of central region of a bipod and the corresponding two-dimensional atomic simulation, demonstrating the occurrence of the ZB structure.

small ZnO seeds. The pure ZnO seeds, the majority of which are less than 3 nm in diameter, have WZ structure (Figure S19 (Supporting Information)). Next, a solution containing 0.5 mmol of $Mg(St)_2$ was introduced into the reaction flask. The reaction was extended for another 4 min. As shown in Figure 11, the addition of $Mg(St)_2$ solution modified the pure ZnO seeds by creating domains with ZB phase which eventually resulted in the growth of tetrapods with long arms (see additional data in Figure S20 (Supporting Information)). Note that activation of the Mg precursor by alcohol takes several minutes due to the low reactivity of $Mg(St)_2$, which has been demonstrated by FTIR analyses (Figure 1J). The effective concentration of the Mg precursor in the time scale of one or two minutes after the injection of the $Mg(St)_2$ solution is significantly lower than that of the Zn precursor. Therefore, the occurrence of ZB phase in the seeded growth experiment is consistent with the formation of the initial growth seeds with ZB cores in the 5% $Mg(St)_2$ reaction in which the concentration of the Zn precursor is much higher than that of the Mg precursor. The seeded growth experiment demonstrates that, at the primary growth stage, the incorporation of Mg^{2+} ions into the ZnO host lattices is much more complex than simple substitution. The introduction of specific dopant ions in the reaction system may significantly influence the growth of the host lattices by modifying the crystallographic phase of the ZnO seeds, which eventually leads to doped nanocrystals with different morphologies.

Surface Ligands. This subsection aims to study the surface ligands of the doped ZnO nanocrystals. Apart from the crystallographic phase of the initial growth seeds, surface ligands that selectively bond onto certain surfaces of nanocrystals are another important factor that influences the formation of nanocrystals. In a previous work associated with the synthesis of pure ZnO nanocrystals, Knoll et al. demonstrated that ZnO nanotetrapods were obtained by tuning the amount of capping agents, oleic acid, in the reactions.[67] The surfactant-assisted growth was suggested to be the main mechanism of the synthetic strategy for the ZnO tetrapods.

In this regard, surface ligands of the nanocrystals, i.e. faceted particles, tetrapods and ultrathin nanowires from the 0%, 5% and 50% $Mg(St)_2$ reactions, respectively, were characterized by FTIR. The nanocrystals were purified by successive methanol extraction and extensive washing to remove the organic impurities, only leaving ligands that directly bond to the surfaces of the nanocrystals. FTIR results (Figure S21 (Supporting Information)) show that $R\text{-}COO^-$ is the surface ligand for the resulting nanocrystals.[48,51] Considering that no additional surfactants are used in our reactions, we conclude that stearate ions (St^-) are the surface ligands for both the pure ZnO nanocrystals and the Mg-doped ZnO nanocrystals. This is supported by the proton

(67) Zhong, X. H.; Feng, Y. Y.; Zhang, Y. L.; Lieberwirth, I.; Knoll, W. G. *Small* **2007**, *3*, 1194–1199.

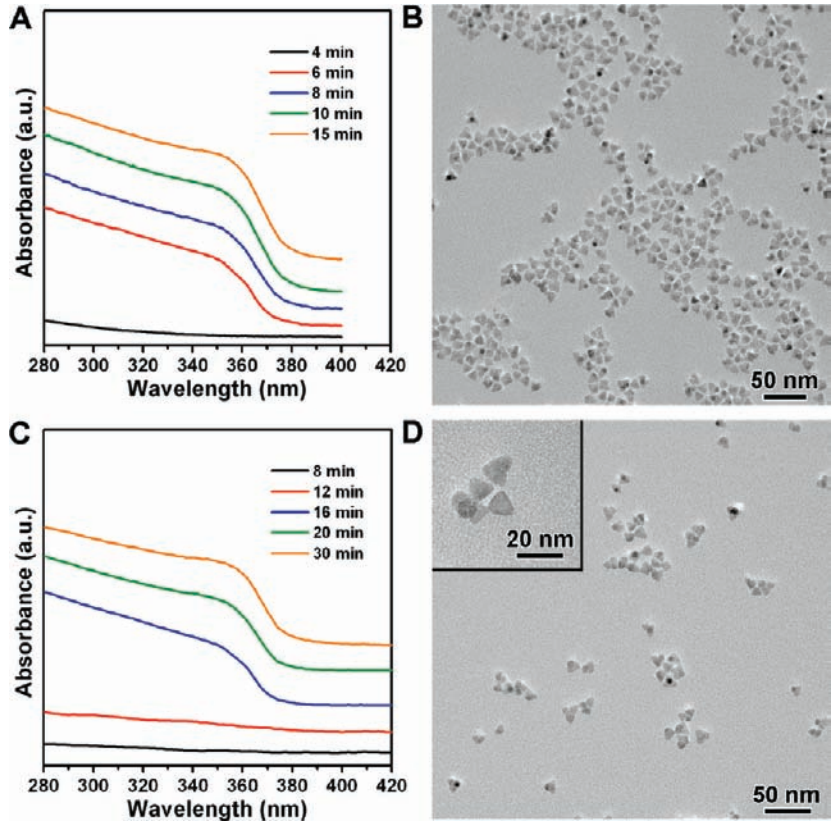

Figure 12. Control experiments for the 5% and 50% $Mg(St)_2$ reactions, in which the dopant precursors are replaced by HSt. (A) Temporal evolution of UV−vis spectra, and (B) a typical TEM image of the nanocrystals from the reaction starting with 0.95 mmol of $Zn(St)_2$ and 0.1 mmol of HSt. (C) Temporal evolution of UV−vis spectra, and (D) a typical TEM image of the nanocrystals from the reaction starting with 0.5 mmol of $Zn(St)_2$ and 1 mmol of HSt (Inset is a corresponding higher-magnification TEM image).

nuclear magnetic resonance (^{1}H NMR) investigations on the pure ZnO nanocrystals by Peng and co-workers.[48]

We carried out two set of control experiments for the 5% and 50% $Mg(St)_2$ reactions to study the impacts of surface ligands on the formation of doped nanocrystals. The first set of control experiments is designed to replace the dopant precursor, $Mg(St)_2$ with stearic acid (HSt). The reagents of the control experiments for the 5% and 50% $Mg(St)_2$ reactions are 0.95 mmol of $Zn(St)_2$ and 0.1 mmol of HSt, and 0.5 mmol of $Zn(St)_2$ and 1 mmol of HSt, respectively. As shown in Figure 12, B and D, the resulting nanocrystals for both experiments are faceted particles, similar to the pure ZnO nanocrystals from the 0% $Mg(St)_2$ reaction. Another feature of this set of control experiments is that the introduction of additional fatty acid as free ligands significantly slows the formation of nanocrystals. Time-dependent UV−vis spectra of the aliquots taken from the control experiment for the 50% $Mg(St)_2$ reaction indicated that when 1 mmol of HSt was involved in the reaction, the absorbance peak of the ZnO nanocrystals could not be detected until the reaction was lasted for 16 min (Figure 12C), much longer than that for the reaction without additional fatty acid. This fact can be explained by the ligand effects on the monomer reactivity. The additional HSt dissolves ZnO nanocrystals at elevated temperatures, hindering the formation of ZnO crystals.[48] In this sense, fatty acids act as the prohibiting reagents for the formation of oxide nanocrystals, as observed in some other systems, such as iron oxide.[68] In the second set of control experiments for the 5% and 50% $Mg(St)_2$ reactions, different amounts (0.1 and 0.5 mmol) of additional HSt were introduced into the reagents. For instance, one of the control experiments for the 50% $Mg(St)_2$ reaction started with 0.5 mmol of $Zn(St)_2$, 0.5 mmol of $Mg(St)_2$ and 0.5 mmol of HSt. As shown in Figure S22 (Supporting Information), tetrapods and ultrathin nanowires were obtained in the control experiments for the 5% and 50% $Mg(St)_2$ reactions, respectively. This indicates that in the presence of dopant precursor, the introduction of suitable amounts of additional ligands does not affect the shapes of the resulting doped nanocrystals.

Solvents, the organic mediums used for the syntheses of nanocrystals, sometimes may also participate in the reactions, acting as surfactant like reagents.[49] In this regard, we replaced ODE, the solvent, by *n*-octadecane, a high boiling-point noncoordinating alkane. Results (Figure S23 (Supporting Information)) show that the resulting doped nanocrystals are almost identical to those from the reactions with ODE as solvent, implying that use of ODE as solvent does not account for the formation of doped nanocrystals with defined shapes.

In short, we conclude that stearate ions are the ligands that directly bond onto the surfaces of the doped ZnO nanocrystals. Surface ligands play an important role for the syntheses of oxide nanocrystals. Additional ligands of fatty acid significantly slow the reactions and vary the reactivity of metal precursors. Nevertheless, we suggest that in our synthetic systems, the shapes of doped nanocrystals are mainly determined by the crystal structures of the initial growth seeds. Introduction of suitable amounts of additional fatty acids in the reagents does not change the shapes of the resulting doped nanocrystals. As

(68) Zhao, F.; Rutherford, M.; Grisham, S. Y.; Peng, X. *J. Am. Chem. Soc.* **2009**, *131*, 5350–5358.

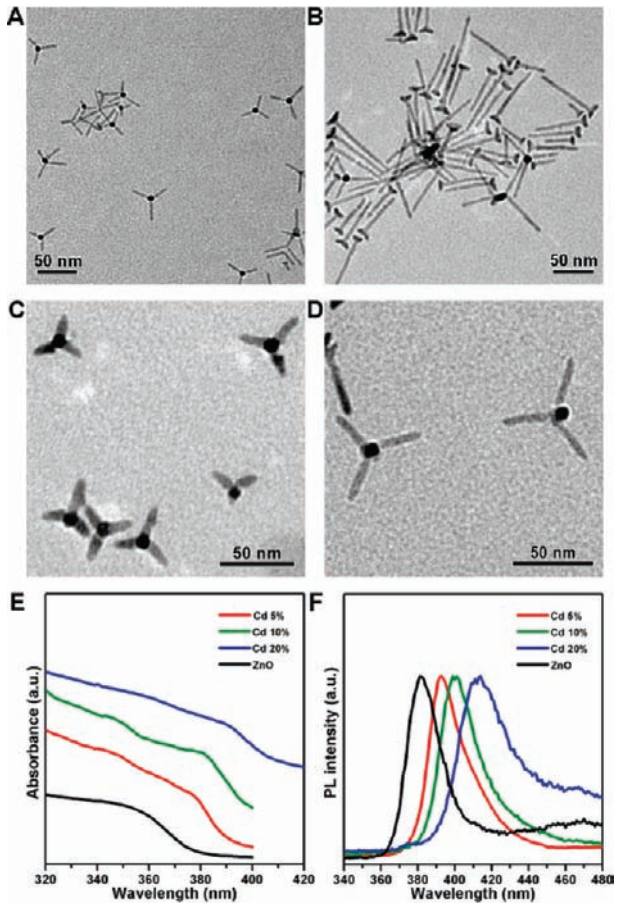

Figure 13. Cd, Mn or Ni-doped ZnO nanocrystals. (A) A typical TEM image of the Cd-doped ZnO nanotetrapods. 0.1 mmol of $Cd(Ac)_2 \cdot 2H_2O$ and 0.9 mmol of $Zn(St)_2$ were used as starting materials. (B) A typical TEM image of the Cd-doped ZnO nanowires. 0.2 mmol of $Cd(Ac)_2 \cdot 2H_2O$ and 0.8 mmol of $Zn(St)_2$ were used as starting materials. (C) A typical TEM image of the Mn-doped ZnO nanotetrapods. 0.1 mmol of $Mn(Ac)_2$ and 0.9 mmol of $Zn(St)_2$ were used as starting materials. (D) A typical TEM image of the Ni-doped ZnO nanotetrapods. 0.05 mmol of $Ni(St)_2$ and 0.95 mmol of $Zn(St)_2$ were used as starting materials. (E) and (F) UV−vis absorption and photoluminescence spectra (excited at 300 nm) of the Cd-doped ZnO nanocrystals with various molar ratios of the Cd precursor in the starting materials. The spectra of pure ZnO nanocrystals are also shown for comparison.

suggested by one of the reviewers, the presence of surface ligands may govern the directional growth of the doped nanocrystals after the formation of initial growth seeds. Further experiments or theoretical simulations are desired to verify this postulation.

ZnO Nanocrystals Doped with Cd, Mn or Ni. The doping procedure based on the Mg-doped ZnO nanocrystals is readily extended to other doped ZnO nanocrystals since the alcoholysis approach has been demonstrated to be effective for synthesizing a number of oxide nanocrystals. The properties of dopant ions can be partly reflected by the corresponding oxides. Therefore we select a few divalent ions, Cd^{2+}, which is a post-transition metal ion, Mn^{2+} and Ni^{2+}, which are transition metal ions, as dopants to examine the doping effects on the shapes of the doped ZnO nanocrystals. These dopant ions are chosen because their corresponding oxides adopt rock-salt type of cubic crystal structure with same space group and comparable lattice parameters, as revealed by Figure S24 (Supporting Information).

Preliminary findings are encouraging. Similar to that of the Mg-doped ZnO nanocrystals, Cd-doped ZnO nanotetrapods

Scheme 1. Growth Paths of the Zn−Mg−O Nanocrystals with Defined Shapes

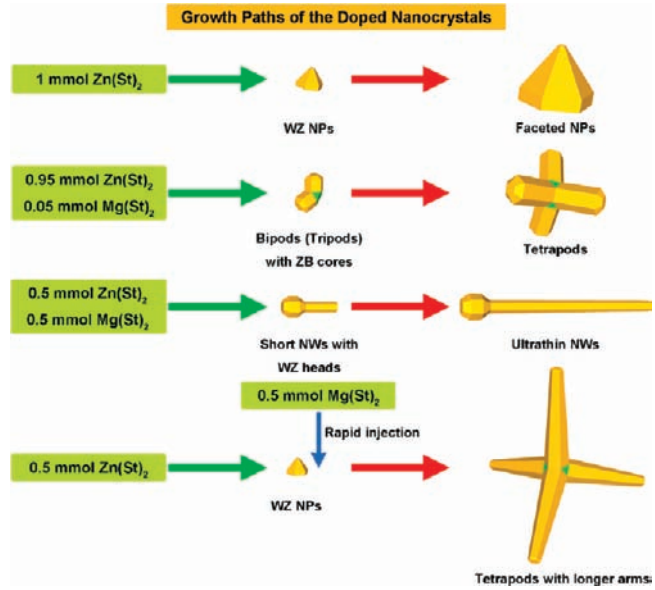

(Figure 13A) were obtained when the reaction started with a low concentration, 10 mol %, of the Cd precursor in the reagents. Increasing the relative concentration of the Cd precursor to 20 mol % resulted in the growth of Cd-doped ZnO nanowires (Figure 13B). UV−vis absorption and PL measurements show that the optical bandgap of the Cd-doped ZnO nanocrystals can be tuned from 3.3 to 3.0 eV by varying the relative concentrations of the Cd precursor in the reagents (Figure 13, E and F). As shown in Figure 13, C and D, Mn-doped ZnO nanotetrapods and Ni-doped ZnO nanotetrapods, which are of interest as building blocks for nanospintronic devices, were generated by using 0.1 mmol of $Mn(Ac)_2$ and 0.9 mmol of $Zn(St)_2$, and 0.05 mmol of $Ni(St)_2$ and 0.95 of mmol $Zn(St)_2$ as starting materials, respectively. These results confirm that the introduction of specific dopants in the syntheses may significantly influence the shapes of the resulting doped ZnO nanocrystals. Investigations aiming to optimize the syntheses of doped ZnO nanocrystals and utilize the doped ZnO nanocrystals for device application are ongoing and results shall be reported in subsequent publications.

Conclusions

As summarized in Scheme 1, we demonstrate that the introduction of Mg dopants is critical for the dramatic shape evolution of the Mg-doped ZnO nanocrystals. High quality Mg-doped ZnO nanocrystals with well-defined shapes, from tetrapods to ultrathin nanowires, which exhibit tunable optoelectronic properties, are obtained for the first time. Mechanism studies show that at the primary growth stage, the incorporation of Mg^{2+} ions into the ZnO seeds significantly influences the growth of the host lattices. The relative concentration of dopant precursor in the reagents is one of the key factors that result in initial growth seeds with different crystallographic phases and shapes, which eventually lead to doped nanocrystals with different morphologies. We verify that stearate ions are the ligands that bond onto the surfaces of the doped nanocrystals. Additional ligands of fatty acids play an important role for the formation of nanocrystals, in terms of tuning the reactivity of metal precursors.

The simple doping scheme based on the Mg-doped ZnO nanocrystals is readily applied to ZnO nanocrystals doped with

other ions, such as Cd^{2+}, Mn^{2+} and Ni^{2+}. A great benefit of the doping procedure we have developed is that doped ZnO nanocrystals with exactly defined compositions, specifically tailored shapes and advanced materials properties, which are advantageous for fully exploiting the potential of these novel materials, may be designed and achieved by judiciously adjusting precursor choices, manipulating relative concentrations of the dopant precursors and optimizing reaction parameters in the syntheses.

Acknowledgment. The work was financially supported by the Zi Jin program of Zhejiang University, Qian Jiang Foundation of Zhejiang Province under Grant No. QJD0702004, National Natural Science Foundation of China under Grant No. 50802085, and National Basic Research Program of China (973 Program) under Grant No. 2006CB604906. We thank Prof. Sir Harold W. Kroto (Florida State University, U.S.A.), Prof. Xiaogang Peng (Zhejiang University, China), Prof. Chao Gao (Zhejiang University, China), Prof. Xiaogang Liu (National University of Singapore, Singapore), Prof. Ze Zhang (Zhejiang University, China), Dr. Fei Zhao (University of Arkansas, U.S.A.), Prof. Baoquan Sun (Soochow University, China), Prof. Youyong Li (Soochow University, China), Prof. Xiaobin Zhang (Zhejiang University, China) and Dr. Jianpu Wang (University of Cambridge, UK) for many inspiring discussions and Dr. Bo Wu (Institute of Metal Research, Chinese Academy of Sciences, China), Prof. Xiaoqing Pan (University of Michigan, U.S.A.) and Prof. Toru Maekawa (Toyo University, Japan) for assistance with the TEM techniques.

Supporting Information Available: Additional TEM and HRTEM images, XPS, STEM, EDX, and PL results for selected samples, ICP-AAS data, details of the quantitative etching experiments, temporal evolution of UV−vis and morphologies for tetrapods and ultrathin nanowires, scheme of the seeded growth experiment, FTIR spectra of the purified oxide nanocrystals, control experiments with additional ligands and without dopant precursors, control experiments with both additional ligands and dopant precursors, control experiments with different solvents, three-dimensional models for the corresponding oxides, and a complete list of authors for reference 24. This material is available free of charge via the Internet at http://pubs.acs.org.

JA103956P